Letter

Large inverted band gap in strained three-layer InAs/GaInSb quantum wells

C. Avogadri,[1] S. Gebert,[1,2] S. S. Krishtopenko,[1] I. Castillo,[1] C. Consejo,[1] S. Ruffenach,[1] C. Roblin,[1] C. Bray,[1] Y. Krupko,[1] S. Juillaguet,[1] S. Contreras,[1] A. Wolf,[3] F. Hartmann,[3] S. Höfling,[3] G. Boissier,[2] J.-B. Rodriguez,[2] S. Nanot,[1] E. Tournié,[2] F. Teppe,[1,*] and B. Jouault[1,†]

[1]*Laboratoire Charles Coulomb (L2C), UMR 5221 CNRS–Université de Montpellier, Montpellier, France*
[2]*Institut d'Electronique et des Systèmes (IES), UMR 5214 CNRS–Université de Montpellier, Montpellier, France*
[3]*Technische Physik, Physikalisches Institut and Würzburg-Dresden Cluster of Excellence ct.qmat, Am Hubland, D-97074 Würzburg, Germany*

(Received 7 March 2022; accepted 16 September 2022; published 5 December 2022)

Quantum spin Hall insulators (QSHIs) based on HgTe and three-layer InAs/GaSb quantum wells (QWs) have comparable bulk band gaps of about 10–18 meV. The former, however, features a band gap vanishing with temperature, while the gap in InAs/GaSb QSHIs is rather temperature independent. Here, we report on the realization of a large inverted band gap in strained three-layer InAs/GaInSb QWs. By temperature-dependent magnetotransport measurements of gated Hall bar devices, we extract a gap as high as 45 meV. By combining local and nonlocal measurements, we detect edge conductivity at temperatures up to 40 K, possibly of topological origin, with equilibrium lengths of a few micrometers. Our results pave the way for the manipulation of topological edge states at high temperatures in QW heterostructures.

DOI: 10.1103/PhysRevResearch.4.L042042

Introduction. Time-reversal invariant two-dimensional (2D) topological insulators, also known as quantum spin Hall insulators (QSHIs), are characterized by insulating bulk and spin-polarized topologically protected states at the sample edges [1,2]. The presence of these edge states is of great interest for potential applications in spintronics, metrology [3], and quantum information [4,5]. So far, the QSHI state was experimentally established in HgTe quantum wells (QWs) [6], InAs/GaSb QW bilayers [7,8] and $1T'$-WTe_2 monolayers [9]. The latter with its 45-meV inverted band gap [10,11] demonstrated a stable QSHI state up to 100 K. This motivates the search of other 2D systems with even wider inverted band gaps, but the observation of QSHI in monolayer systems is experimentally challenging because of structural or chemical instabilities [12–14] and nonmature technological processing. This stimulates the search for alternative candidates for high-temperature QSHIs among QW heterostructures.

The first measurements of the quantized edge conductance (the main characteristic of QSHI) in HgTe QWs were performed at temperatures lower than 2 K [6]. Indeed, a relatively small inverted band gap (typically lower than 15 meV) in HgTe QWs grown on CdTe buffer makes it difficult to observe the quantized edge conductance at elevated temperatures. Note that strain engineering using a virtual substrate increases the band gap up to 55 meV in compressively strained QWs [15]. Such high values, however, occur at low temperatures only, whereas increasing temperature yields the band-gap vanishing and topological phase transition into trivial state [16–20]. Hence, the observation of the QSHI state in HgTe Qws is so far limited to 15 K [21].

QSHIs based on InAs/GaSb QW bilayers raise a considerable interest over HgTe QWs due to their ease of fabrication. However, their small inverted band gap of about 3–4 meV induces a large residual bulk conductance [22]. This limits the observation of quantized edge conductance values to the millikelvin temperature range [8,23–25]. Although the residual bulk conductance can be indeed reduced by means of various techniques (implantation of Si impurities at the InAs/GaSb interface [26], Be doping [27], or the use of a low-purity Ga source for molecular beam epitaxy growth [28]), the quantized values of edge conductance out of the millikelvin range have not yet been observed even in strained InAs/GaInSb QW bilayers with a higher band gap [25,29,30].

Removing the structure inversion asymmetry inherent to InAs/GaSb QW bilayers by adding a second InAs layer significantly enhances the inverted band-gap energy [31], resulting in a QSHI with the bulk gap comparable with that of inverted HgTe QWs. Despite the general similarities and characteristics of topological states in HgTe QWs [17] and three-layer (3L) InAs/GaSb (QWs) [31–34], the inverted band gap of the latter is rather temperature independent [35,36]. This fact, as well as the theoretically predicted inverted band gap in strained 3L InAs/GaInSb QWs above 60 meV [31], make these QWs extremely attractive for observing quantized edge conductance at high temperatures.

This work reports on the experimental realization of strained 3L InAs/GaInSb QWs with large inverted band gap.

*frederic.teppe@umontpellier.fr
†benoit.jouault@umontpellier.fr

TABLE I. Main sample parameters. For all fabricated Hall bars, W is the width, ℓ_p is the distance between the lateral probes, and l_1 is the distance between the source (or drain) contact and the closest lateral probe.

Sample	InAs thickness (nm)	$Ga_{1-x}In_xSb$ thickness (nm)	Outer barriers	Metamorphic buffer	Device index (W, ℓ_p, l_1 in μm)	Δ theory (meV)	Δ expt. (meV)
S3054	10.3	4.3 ($x = 0.00$)	$Al_{0.9}Ga_{0.1}As_{0.07}Sb_{0.93}$	GaSb	HB0 (10,22,17)	14	N/A
S3052	7.5	3.1 ($x = 0.35$)	$Al_{0.9}Ga_{0.1}As_{0.07}Sb_{0.93}$	AlSb	HB1 (100,220,170)	30	30 ± 2
S3198	7.5	3.1 ($x = 0.35$)	AlSb	AlSb	HB4 (20,10,40), HB6 (20,30,30)	45	45 ± 9

Temperature-dependent magnetotransport measurements of Hall bar devices made from 3L InAs/$Ga_{0.65}In_{0.35}Sb$ QWs in local and nonlocal geometries reveal energy gaps as high as 45 meV, associated with edge conductance attributed to topological states. Note that the experimental gap values can be further enhanced by growing 3L InAs/$Ga_{1-x}In_xSb$ QWs with higher values of x (cf. Ref. [30]).

Materials and methods. We have fabricated a set of three QWs—S3054, S3052, and S3198—with distinct strain and thickness parameters (see Table I). The samples were grown by molecular beam epitaxy. The active part of the samples sketched in Fig. 1(a) contains a symmetric 3L InAs/$Ga_{1-x}In_xSb$ QW embedded between AlGaAsSb barriers. For the samples S3052 and S3198, the widths of the InAs and $Ga_{0.65}In_{0.35}Sb$ layers were chosen to be 25 and 10 monolayers, respectively. For the sample S3054, the width of the InAs and GaSb layers was increased up to 34 and 14 monolayers, respectively. Both samples S3054 and S3052 were grown on semi-insulating GaAs(001) substrates, whereas sample S3198 was grown on a GaSb(001) substrate. The samples have also different metamorphic buffer layers, and different strain states, as discussed in the Supplemental Material [37].

All the samples were processed by optical lithography into micrometer-sized Hall bar devices with a metallic front gate, on a plasma-enhanced chemical vapor deposited 300-nm-thick SiO_2 for samples S3052 and on a 110-nm-thick stacking of SiO_2/Si_3N_4 dielectric insulators for S3054 and S3198. Transport measurements of various gated Hall bars (see Table I) were performed in a cryostat equipped either with a variable temperature insert or with a helium-3 insert for the temperatures below 1.7 K. We used standard lock-in measurements with 10 nA currents at 11 Hz and high-impedance 1 T Ω preamplifiers. The quantity $R_{ij,kl}$ corresponds to the voltage between the probes k and l divided by the current flowing between contacts i and j.

Bulk band gap. Figures 1(c) and 1(f) represent realistic band structure calculations [31]. All the samples have an inverted band structure with the holelike $H1$ band lying above the electronlike $E1$ band [37]. The calculated band gap for the samples S3052 and S3198 is $\Delta \simeq 30$ and 45 meV, respectively. Here, we note an influence of the outer barriers on the band structure of 3L InAs/GaInSb QWs at given layer thicknesses. The sample S3054 with the smaller gap ($\Delta \simeq 14$ meV) is similar to the one studied in Ref. [35], in which the inverted band structure was evidenced.

We first focus on measuring the longitudinal resistivity $\rho_{xx} \simeq R_{14,23} W/\ell_p$ as a function of the gate voltage V_g. Here, ℓ_p is the distance between the lateral probes. In the HB0 device, $\rho_{xx}(V_g)$ displays a peak at $T = 2$ K, indicating a gap opening. However, this peak culminates at $\rho_{xx} \simeq 4.8$ kΩ only with a weak insulating behavior as shown in Fig. 2(b). Thus, the band gap in the HB0 device is shunted either by edge states or a parasitic conductivity channel in one of the cap or buffer layers [37]. Further, we focus mainly on the HB6 device (S3198 sample). Figure 2(a) shows $\rho_{xx}(V_g)$ for the HB6 device, which evidences a much higher peak of around 25 kΩ at low temperature. For clarity, each curve has been horizontally offset by the position of the peak maximum $V_g^{\max}$. The $V_g^{\max}$ values depend on several parameters: amplitude, rate, and direction of the gate voltage sweep, and temperature. In Fig. 2(a), $V_g^{\max} = -7.5$ V at low T. For the other presented devices, $V_g^{\max} = -0.6$, -6, and -8 V at low T for HB0, HB1, and HB4, respectively.

The main peak is flanked on its left side by a dip around $V_g - V_g^{\max} = -2.5$ V. Such local ρ_{xx} minimum can be attributed to the Van Hove singularity at the top of the valence band as seen in Fig. 1(d). Similar dips were also observed in InAs/GaSb QW bilayers [38–40], and recently in 3L InAs/GaSb QWs [36].

Figure 2(c) shows the transverse magnetoresistance ρ_{xy} for the HB6 device at $T = 300$ mK. An ambipolar behavior

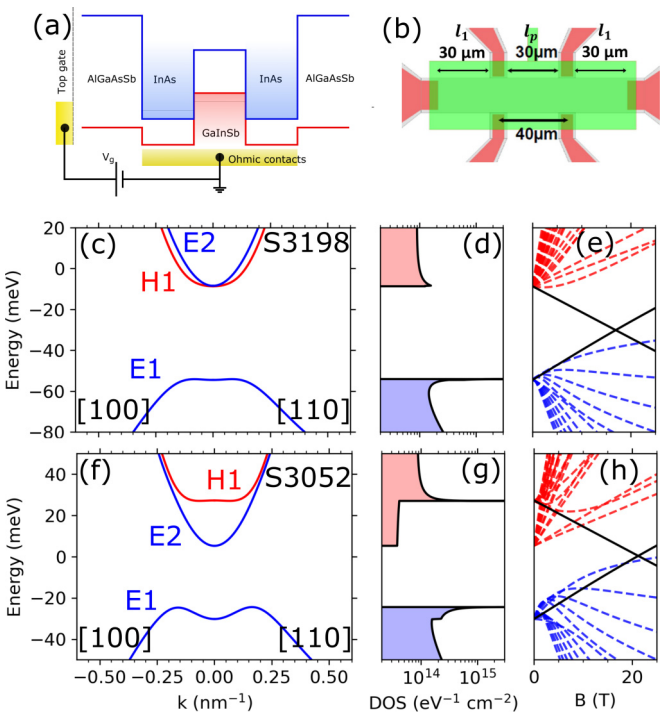

FIG. 1. (a) Qualitative scheme of 3L QWs. (b) Sketch of the Hall bar HB6. (c)–(g) Band structure, density of states, and Landau levels for samples S3198 (c)–(e) and S3052 (e)–(g). The zero-mode Landau levels [6,31] in panels (e) and (h) are indicated by black solid lines.

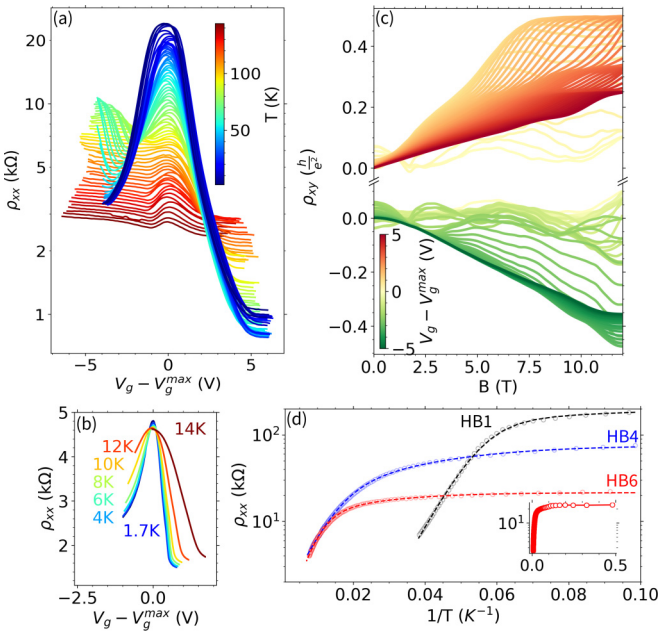

FIG. 2. (a), (b) Longitudinal resistivity $\rho_{xx}(V_g)$ at different temperatures for the HB6 (a) and the HB0 device (b). (c) Transverse magnetoresistance $\rho_{xy}(B)$ as a function of V_g at $T = 300$ mK for the HB6 device. For clarity, a vertical voltage offset has been introduced between $V > V_g^{\max}$ and $V \leqslant V_g^{\max}$. (d) Temperature dependence of the peak resistivity $\rho_{xx}^{\max}$ for the three devices: HB1 (S3052), HB4 (S3198), and HB6 (S3198). Open symbols correspond to the experimental values, while the dashed curves represent the fits as indicated in the text. The inset shows the saturation of $\rho_{xx}^{\max}$ for the HB6 device at lower temperatures down to 2 K (same axes as the main panel).

centered at $V_g = V_g^{\max}$ is evident. In the conduction band (CB), ρ_{xy} is linear at low B with a pronounced quantum Hall effect at high magnetic field. In the valence band (VB), ρ_{xy} is bent below $B = 2$ T even at the lowest available gate voltage, $V_g - V_g^{\max} = -5$ V. At this voltage, both longitudinal and transverse magnetoresistances are satisfactorily fitted by taking into account two types of carriers: holelike carriers of density $n_h = 7.0\times10^{11}$ cm^{-2} and mobility $\mu_h \simeq 1000$ cm^2/V s, and electronlike carriers of density $n_e = 0.4\times10^{11}$ cm^{-2} and mobility $\mu_e \simeq 10\,000$ cm^2/V s. This agrees well with the band structure near the top of the VB, where the Fermi surface has two distinct contours: an inner contour representing electronlike particles and an outer contour corresponding to holelike particles [see Fig. 1(c)]. In accordance with the band structure calculations shown in Fig. 1(e), the occupied low-indices Landau levels at $B > 2$ T are formed by the outer contour states, while the states of the inner contour become depopulated. Experimentally, the measurements of Shubnikov–de Haas (SdH) oscillations at $V_g - V_g^{\max} = -5$ V reveal a single frequency above $B = 5$ T corresponding to the carrier concentration $n_{\rm SdH} = 8.3\times10^{11}$ cm^{-2}. This value corresponds roughly to $n_h + n_e \simeq 7.4\times10^{11}$ cm^{-2}, as obtained from the low-field analysis.

Figure 2(d) summarizes the temperature dependence of the peak value of the resistivity, $\rho_{xx}^{\max}$, for three Hall bar devices: HB1 (S3052), HB4, and HB6 (S3198). At high temperatures (above 25 K for S3052 and 150 K for S3198), the samples demonstrate an additional planar conduction, therefore the corresponding data were discarded. At lower temperatures, a strong increase of $\rho_{xx}^{\max}$ was observed, followed by a weaker temperature dependence at even lower T. The latter is typically attributed to disorder-induced localization gap or edge states, while the strong temperature dependence is associated with thermal activation through the band gap. Note that a similar behavior of $\rho_{xx}^{\max}(T)$ has been commonly observed in inverted InAs/Ga(In)Sb QW bilayers [24,30,41,42].

As seen from Fig. 2(d), $\rho_{xx}^{\max}$ as a function of T is well fitted by the sum of two activation processes with an additional constant term [30]: $(\rho_{xx}^{\max})^{-1} = \sigma_a \exp(-\Delta/2k_BT) + \sigma_{\rm loc}\exp(-\Delta_{\rm loc}/k_BT) + \sigma_0$, where k_B is the Boltzmann constant and σ_0, σ_a, and $\sigma_{\rm loc}$ (Δ and $\Delta_{\rm loc}$) have the dimensions of conductivity (energy). As we impose $\Delta_{\rm loc} < \Delta$, the term $\sigma_a \exp(-\Delta/2k_BT)$ represents the strong T dependence, while the two other terms describe weak temperature dependence in the saturation regime. The fits give the energies $\Delta = 45 \pm 9$ meV for S3198 (HB4 and HB6), $\Delta = 30 \pm 1$ meV for S3052 (HB1), and $\Delta_{\rm loc}$ lying in the range 1.3–6 meV for all devices (cf. Ref. [30]). As seen, experimental band-gap energies are in good agreement with their theoretical expectations. Note that the error bar for S3052 is smaller because it does not include the device-to-device variations. The variation in the measured energy gap between HB4 and HB6 may be caused by long-range inhomogeneity due to variations in the strain profile [37].

Nonlocal resistances. As evidenced from the inset in Fig. 2(d), the resistance peak $\rho_{xx}^{\max}$ for the HB6 device saturates and becomes constant below 10 K, where no activation energy can be found. Further, we demonstrate that this saturation is mainly caused by the conductivity via edge states. Figure 3(a) shows the local resistance $R_{14,23}$ as a function of $V_g - V_g^{\max}$ for device HB4 in the temperature range from 3 K up to 80 K. As seen, the peak amplitude is comparable to that shown in Fig. 2(a), while the V_g range is reduced in order to focus on the gap region with the insulating behavior. Figure 3(b) provides the temperature dependence of nonlocal resistance $R_{26,35}$. One can see that at $|V_g - V_g^{\max}| \simeq 1$ V corresponding to the edges of CB and VB, the local resistance starts exceeding the nonlocal one for all the temperatures. At these V_g values, the nonlocal resistance finds its origin in the current spreading in the bulk of the Hall bars: $R_{26,35} \simeq (4\rho/\pi)\exp(-\pi\ell_p/W)$, where $\rho = R_{14,23}W/\ell_p$ is the bulk resistivity. Experimentally, $R_{26,35}/R_{14,23} \simeq 0.1$–$0.3$ in the CB and VB [37], which yields $\ell_p \simeq 12$–17 μm. The latter is in qualitative agreement with the geometry of HB4 when the finite width of the lateral probes (10 μm) is taken into account.

The situation changes significantly when V_g approaches $V_g^{\max}$ corresponding to the middle of the band gap. In this case, $R_{26,35}$ increases and becomes more than twice larger than $R_{14,23}$. That cannot be explained within the model above. A similar increase of $R_{26,35}$ was also observed in the HB1 and HB6 devices. In the HB0 device, even though the nonlocal resistance increases more moderately, it still becomes ten times higher than the evaluation within the current spreading model.

Resistive network model. Nonlocal resistance is often observed in InAs-based QSHIs [24,43–46]. It has been unambiguously related to edge state conduction by combining electric measurements with spatial imaging using

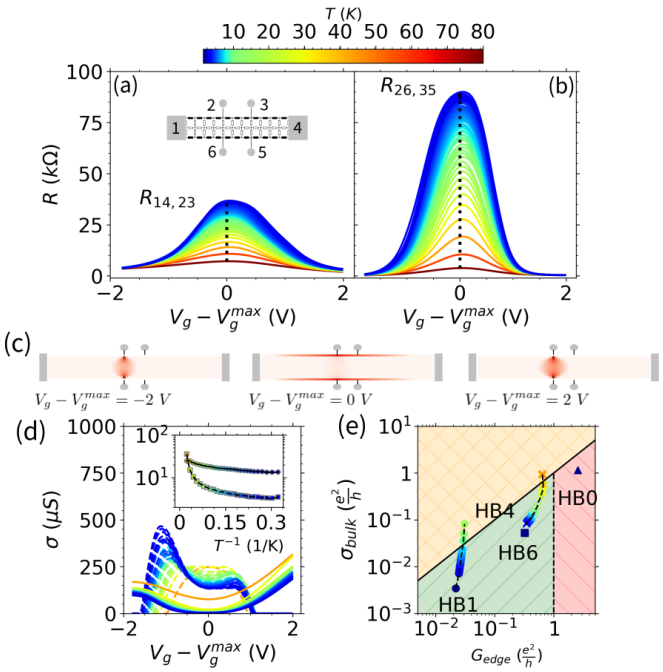

FIG. 3. (a) Local resistance $R_{14,23}$ and (b) nonlocal resistance $R_{26,35}$ for HB4 as a function of $V_g - V_g^{\max}$, at different temperatures from $T = 80$ K down to $T = 3$ K. The inset sketches a minimal resistor square network. (c) Current dissipation calculated in HB4 at three gate voltages, as given by the fitting of $R_{14,23}$ and $R_{26,35}$ by the network model. (d) Fitting parameters ($G_{\rm edge} \times 10$: dotted lines; $\sigma_{\rm bulk}$: solid lines) extracted from panels (a) and (b) for HB4 as a function of $V_g - V_g^{\max}$, at different T. The inset shows $G_{\rm edge}(T)$ and $\sigma_{\rm bulk}(T)$ at $V_g = V_g^{\max}$. (e) $G_{\rm edge}$ and $\sigma_{\rm bulk}$ for HB0 (triangle), HB1 (circle), HB4 (cross), and HB6 (square), at $V_g = V_g^{\max}$ and $T = 3$ K. Solid black line: $\sigma_{\rm bulk} = G_{\rm edge}$. Vertical dashed line: $G_{\rm edge} = e^2/h$ (ballistic edge conduction). Red region: additional parasitic edge conductivity. Green dashed region: diffusive edge conduction. The temperature dependence of $(G_{\rm edge}, \sigma_{\rm bulk})$ is indicated for HB1 (up to 16 K) and HB4 (up to 57 K).

superconducting quantum interference device microscopy [47,48] and scanning tunneling microscopy [49]. To separate the edge and bulk contributions, each Hall bar device was modeled by a 2D resistor square network, parametrized by the edge and bulk conductivities: $\sigma_{\rm edge}$ (in μm/Ω) and $\sigma_{\rm bulk}$ (in $\square/\Omega$) [45]. These two parameters are used to simultaneously fit the local and nonlocal resistances at a given gate voltage, which allows visualizing the resulting current dissipation in the devices [see Fig. 3(c)].

To compare the relative contribution from $\sigma_{\rm edge}$ and $\sigma_{\rm bulk}$ into the resistance measurement, we introduce the edge conductance as $G_{\rm edge} = \sigma_{\rm edge}/\ell_p$. The fitting parameters $G_{\rm edge}$ and $\sigma_{\rm bulk}$ as a function of V_g for the HB4 device are shown in Fig. 3(d). We define the gap region as $\sigma_{\rm bulk} \leqslant 10$ μS at $T \sim 1.8$ K, which corresponds roughly to $|V_g - V_g^{\max}| \lessapprox 1$ V. There, at $T = 1.8$ K, $\sigma_{\rm bulk}$ is about five times smaller than $G_{\rm edge}$ and the edge conductance dominates. On the contrary, $G_{\rm edge}$ vanishes far outside the band-gap region. This disappearance is also observed in HB1 and HB6 [37]. Since such a disappearance is not expected for trivial edge states, this suggests that the edge states are topological in nature. In general, dual gated devices are necessary to manipulate separately both carrier density and electric field, and prove the topological nature of the edge states [50]. However, additional calculations of the band structure in the presence of an external electric field along the growth direction reveal that the large energy gap stabilizes the topological phase over a gate voltage range of ± 25 V, making it likely that these topological edge states persist in the single-gate devices studied.

At the top of the VB, $G_{\rm edge}$ is nonzero and even has a local maximum as seen in Fig. 3(d) when $V_g - V_g^{\max} \simeq -1$ V. Actually, we cannot attribute this phenomenon to possible inhomogeneities of the HB4 device, since the similar behavior is also reproduced in HB6 and HB1. Moreover, the nonzero $G_{\rm edge}$ contribution in the top VB region is not surprising in view of recent theoretical studies predicting the coexistence of edge and bulk states in complex VBs of HgTe QWs [51]. Note that the valence band of our 3L InAs/GaInSb QWs [37] is similar to those of HgTe QWs [17]. Additionally, the inset of Fig. 3(d) shows $G_{\rm edge}$ and $\sigma_{\rm bulk}$ at $V_g = V_g^{\max}$ and confirms the main points of the previous analysis: $\sigma_{\rm bulk}$ has a strong T dependence due to thermal activation above 40 K, while $G_{\rm edge}$ dominates the bulk contribution below 40 K. Clearly, the two curves cross at $T \simeq 40$ K, even if above 40 K, the nonlocal resistance reaches the noise level and $G_{\rm edge}$ cannot be determined anymore [45].

Assuming that the edge states are helical, the edge conductance in the diffusive regime is given by $G_{\rm edge} = (e^2/h)\lambda/\ell_p$, where λ is the characteristic length at which the two counter propagating edge states equilibrate. From $\sigma_{\rm edge}$ at $V_g = V_g^{\max}$ and the lowest temperature, one extracts $\lambda = 24$, 2, 4, and 10 μm for the HB0, HB1, HB4, and HB6 devices, respectively. For the HB0 device, as $\lambda(HB0) = 24$ μm is larger than the distance ℓ_p between the HB0 probes, $G_{\rm edge}(HB0)$ goes beyond the quantum limit e^2/h, and thus cannot be attributed to topological edge states only: additional parasitic edge conduction is at play. By contrast, in HB1, HB4, and HB6 devices, $G_{\rm edge}$ remains smaller than e^2/h, and edge conduction via topological edge states only is possible with λ values comparable to those of the literature [24,52]. One may even suppose that in devices with the largest gap (HB4 and HB6) the topological edge states are less scattered by local potential fluctuations, which may explain why λ is larger in these devices than in HB1. Figure 3(e) summarizes the values of $(\sigma_{\rm bulk}, G_{\rm edge})$ at $V_g = V_g^{\max}$ for all the devices. In the HB0 device, $\sigma_{\rm bulk} \simeq G_{\rm edge}$, and the current flows equally in bulk and edges. By contrast, in the other devices, the current in the band-gap region flows mainly on the edges at $T = 3$ K.

Summary. We have demonstrated a large inverted band gap in strained 3L InAs/GaInSb QWs, whose value is comparable with those in compressively strained HgTe QWs [15] and 1T'-WTe_2 monolayers [9]. The band gap in 3L InAs/GaInSb QWs can be even higher than our reported values [31]. Quantitative analysis of the experimental data evidenced topological edge channels.

Acknowledgments. This work was supported by the Terahertz Occitanie Platform, by CNRS through IRP "TeraMIR," by the French Agence Nationale pour la Recherche (Colector project, EquipEx EXTRA), and by the European Union through the Marie-Curie grant (Agreement No. 765426) from Horizon 2020 research and innovation programme.

[1] C. L. Kane and E. J. Mele, Quantum Spin Hall Effect in Graphene, Phys. Rev. Lett. **95**, 226801 (2005).

[2] B. A. Bernevig, T. L. Hughes, and S.-C. Zhang, Quantum spin Hall effect and topological phase transition in HgTe quantum wells, Science **314**, 1757 (2006).

[3] I. Yahniuk, S. S. Krishtopenko, G. Grabecki, B. Jouault, C. Consejo, W. Desrat, M. Majewicz, A. M. Kadykov, K. E. Spirin, V. I. Gavrilenko, N. N. Mikhailov, S. A. Dvoretsky, D. B. But, F. Teppe, J. Wróbel, G. Cywiński, S. Kret, T. Dietl, and W. Knap, Magneto-transport in inverted HgTe quantum wells, npj Quantum Mater. **4**, 13 (2019).

[4] M. Z. Hasan and C. L. Kane, *Colloquium*: Topological insulators, Rev. Mod. Phys. **82**, 3045 (2010).

[5] X.-L. Qi and S.-C. Zhang, Topological insulators and superconductors, Rev. Mod. Phys. **83**, 1057 (2011).

[6] M. König, S. Wiedmann, C. Brune, A. Roth, H. Buhmann, L. W. Molenkamp, X.-L. Qi, and S.-C. Zhang, Quantum spin Hall insulator state in HgTe quantum wells, Science **318**, 766 (2007).

[7] C. Liu, T. L. Hughes, X.-L. Qi, K. Wang, and S.-C. Zhang, Quantum Spin Hall Effect in Inverted Type-II Semiconductors, Phys. Rev. Lett. **100**, 236601 (2008).

[8] I. Knez, R.-R. Du, and G. Sullivan, Evidence for Helical Edge Modes in Inverted InAs/GaSb Quantum Wells, Phys. Rev. Lett. **107**, 136603 (2011).

[9] S. Wu, V. Fatemi, Q. D. Gibson, K. Watanabe, T. Taniguchi, R. J. Cava, and P. Jarillo-Herrero, Observation of the quantum spin Hall effect up to 100 Kelvin in a monolayer crystal, Science **359**, 76 (2018).

[10] Z. Fei, T. Palomaki, S. Wu, W. Zhao, X. Cai, B. Sun, P. Nguyen, J. Finney, X. Xu, and D. H. Cobden, Edge conduction in monolayer WTe_2, Nat. Phys. **13**, 677 (2017).

[11] S. Tang, C. Zhang, D. Wong, Z. Pedramrazi, H.-Z. Tsai, C. Jia, B. Moritz, M. Claassen, H. Ryu, S. Kahn, J. Jiang, H. Yan, M. Hashimoto, D. Lu, R. G. Moore, C.-C. Hwang, C. Hwang, Z. Hussain, Y. Chen, M. M. Ugeda *et al.*, Quantum spin Hall state in monolayer 1T′-WTe_2, Nat. Phys. **13**, 683 (2017).

[12] Y. Cao, A. Mishchenko, G. L. Yu, E. Khestanova, A. P. Rooney, E. Prestat, A. V. Kretinin, P. Blake, M. B. Shalom, C. Woods, J. Chapman, G. Balakrishnan, I. V. Grigorieva, K. S. Novoselov, B. A. Piot, M. Potemski, K. Watanabe, T. Taniguchi, S. J. Haigh, A. K. Geim *et al.*, Quality heterostructures from two-dimensional crystals unstable in air by their assembly in inert atmosphere, Nano Lett. **15**, 4914 (2015).

[13] L. Wang, I. Gutierrez-Lezama, C. Barreteau, N. Ubrig, E. Giannini, and A. F. Morpurgo, Tuning magnetotransport in a compensated semimetal at the atomic scale, Nat. Commun. **6**, 8892 (2015).

[14] F. Ye, J. Lee, J. Hu, Z. Mao, J. Wei, and P. X.-L. Feng, Environmental instability and degradation of single- and few-layer WTe_2 nanosheets in ambient conditions, Small **12**, 5802 (2016).

[15] P. Leubner, L. Lunczer, C. Brüne, H. Buhmann, and L. W. Molenkamp, Strain Engineering of the Band Gap of HgTe Quantum Wells Using Superlattice Virtual Substrates, Phys. Rev. Lett. **117**, 086403 (2016).

[16] F. Teppe, M. Marcinkiewicz, S. S. Krishtopenko, S. Ruffenach, C. Consejo, A. M. Kadykov, W. Desrat, D. But, W. Knap, J. Ludwig, S. Moon, D. Smirnov, M. Orlita, Z. Jiang, S. V. Morozov, V. I. Gavrilenko, N. N. Mikhailov, and S. A. Dvoretskii, Temperature-driven massless Kane fermions in HgCdTe crystals, Nat. Commun. **7**, 12576 (2016).

[17] S. S. Krishtopenko, I. Yahniuk, D. B. But, V. I. Gavrilenko, W. Knap, and F. Teppe, Pressure- and temperature-driven phase transitions in HgTe quantum wells, Phys. Rev. B **94**, 245402 (2016).

[18] A. V. Ikonnikov, S. S. Krishtopenko, O. Drachenko, M. Goiran, M. S. Zholudev, V. V. Platonov, Y. B. Kudasov, A. S. Korshunov, D. A. Maslov, I. V. Makarov, O. M. Surdin, A. V. Philippov, M. Marcinkiewicz, S. Ruffenach, F. Teppe, W. Knap, N. N. Mikhailov, S. A. Dvoretsky, and V. I. Gavrilenko, Temperature-dependent magnetospectroscopy of HgTe quantum wells, Phys. Rev. B **94**, 155421 (2016).

[19] M. Marcinkiewicz, S. Ruffenach, S. S. Krishtopenko, A. M. Kadykov, C. Consejo, D. B. But, W. Desrat, W. Knap, J. Torres, A. V. Ikonnikov, K. E. Spirin, S. V. Morozov, V. I. Gavrilenko, N. N. Mikhailov, S. A. Dvoretskii, and F. Teppe, Temperature-driven single-valley Dirac fermions in HgTe quantum wells, Phys. Rev. B **96**, 035405 (2017).

[20] A. M. Kadykov, S. S. Krishtopenko, B. Jouault, W. Desrat, W. Knap, S. Ruffenach, C. Consejo, J. Torres, S. V. Morozov, N. N. Mikhailov, S. A. Dvoretskii, and F. Teppe, Temperature-Induced Topological Phase Transition in HgTe Quantum Wells, Phys. Rev. Lett. **120**, 086401 (2018).

[21] K. Bendias, S. Shamim, O. Herrmann, A. Budewitz, P. Shekhar, P. Leubner, J. Kleinlein, E. Bocquillon, H. Buhmann, and L. W. Molenkamp, High mobility HgTe microstructures for quantum spin Hall studies, Nano Lett. **18**, 4831 (2018).

[22] Y. Naveh and B. Laikhtman, Magnetotransport of coupled electron-holes, Europhys. Lett. **55**, 545 (2001).

[23] I. Knez and R.-R. Du, Quantum spin Hall effect in inverted InAs/GaSb quantum wells, Front. Phys. **7**, 200 (2012).

[24] L. Du, I. Knez, G. Sullivan, and R.-R. Du, Robust Helical Edge Transport in Gated InAs/GaSb Bilayers, Phys. Rev. Lett. **114**, 096802 (2015).

[25] L. Du, T. Li, W. Lou, X. Wu, X. Liu, Z. Han, C. Zhang, G. Sullivan, A. Ikhlassi, K. Chang, and R.-R. Du, Tuning Edge States in Strained Layer InAs/GaInSb Quantum Spin Hall Insulators, Phys. Rev. Lett. **119**, 056803 (2017).

[26] I. Knez, C. T. Rettner, S.-H. Yang, S. S. P. Parkin, L. Du, R.-R. Du, and G. Sullivan, Observation of Edge Transport in the Disordered Regime of Topologically Insulating InAs/GaSb Quantum Wells, Phys. Rev. Lett. **112**, 026602 (2014).

[27] K. Suzuki, Y. Harada, K. Onomitsu, and K. Muraki, Gate-controlled semimetal-topological insulator transition in an InAs/GaSb heterostructure, Phys. Rev. B **91**, 245309 (2015).

[28] C. Charpentier, S. Fält, C. Reichl, F. Nichele, A. N. Pal, P. Pietsch, T. Ihn, K. Ensslin, and W. Wegscheider, Suppression of bulk conductivity in InAs/GaSb broken gap composite quantum wells, Appl. Phys. Lett. **103**, 112102 (2013).

[29] T. Akiho, F. Couëdo, H. Irie, K. Suzuki, K. Onomitsu, and K. Muraki, Engineering quantum spin Hall insulators by strained-layer heterostructures, Appl. Phys. Lett. **109**, 192105 (2016).

[30] H. Irie, T. Akiho, F. Couëdo, K. Suzuki, K. Onomitsu, and K. Muraki, Energy gap tuning and gate-controlled topological phase transition in InAs/$In_xGa_{1-x}Sb$ composite quantum wells, Phys. Rev. Mater. **4**, 104201 (2020).

[31] S. S. Krishtopenko and F. Teppe, Quantum spin Hall insulator with a large bandgap, Dirac fermions, and bilayer graphene analog, Sci. Adv. **4**, eaap7529 (2018).

[32] S. Ruffenach, S. S. Krishtopenko, L. S. Bovkun, A. V. Ikonnikov, M. Marcinkiewicz, C. Consejo, M. Potemski, B.

Piot, M. Orlita, B. R. Semyagin, M. A. Putyato, E. A. Emel'yanov, V. V. Preobrazhenskii, W. Knap, F. Gonzalez-Posada, G. Boissier, E. Tournié, F. Teppe, and V. I. Gavrilenko, Magnetoabsorption of Dirac fermions in InAs/GaSb/InAs "three-layer" gapless quantum wells, JETP Lett. **106**, 727 (2017).

[33] S. S. Krishtopenko, S. Ruffenach, F. Gonzalez-Posada, C. Consejo, W. Desrat, B. Jouault, W. Knap, M. A. Fadeev, A. M. Kadykov, V. V. Rumyantsev, S. V. Morozov, G. Boissier, E. Tournié, V. I. Gavrilenko, and F. Teppe, Terahertz spectroscopy of two-dimensional semimetal in three-layer InAs/GaSb/InAs quantum well, JETP Lett. **109**, 96 (2019).

[34] S. S. Krishtopenko, W. Desrat, K. E. Spirin, C. Consejo, S. Ruffenach, F. Gonzalez-Posada, B. Jouault, W. Knap, K. V. Maremyanin, V. I. Gavrilenko, G. Boissier, J. Torres, M. Zaknoune, E. Tournié, and F. Teppe, Massless Dirac fermions in III-V semiconductor quantum wells, Phys. Rev. B **99**, 121405(R) (2019).

[35] S. S. Krishtopenko, S. Ruffenach, F. Gonzalez-Posada, G. Boissier, M. Marcinkiewicz, M. A. Fadeev, A. M. Kadykov, V. V. Rumyantsev, S. V. Morozov, V. I. Gavrilenko, C. Consejo, W. Desrat, B. Jouault, W. Knap, E. Tournié, and F. Teppe, Temperature-dependent terahertz spectroscopy of inverted-band three-layer InAs/GaSb/InAs quantum well, Phys. Rev. B **97**, 245419 (2018).

[36] M. Meyer, S. Schmid, F. Jabeen, G. Bastard, F. Hartmann, and S. Höfling, Topological band structure in InAs/GaSb/InAs triple quantum wells, Phys. Rev. B **104**, 085301 (2021).

[37] See Supplemental Material at http://link.aps.org/supplemental/10.1103/PhysRevResearch.4.L042042 for details of band structure calculations, the growth scheme of the samples, fitting of $\rho_{xx}^{\max}(T)$, and the resistive network model.

[38] M. J. Yang, C. H. Yang, B. R. Bennett, and B. V. Shanabrook, Evidence of a Hybridization Gap in "Semimetallic" InAs/GaSb Systems, Phys. Rev. Lett. **78**, 4613 (1997).

[39] I. Brihuega, P. Mallet, H. González-Herrero, G. Trambly de Laissardière, M. M. Ugeda, L. Magaud, J. M. Gómez-Rodríguez, F. Ynduráin, and J.-Y. Veuillen, Unraveling the Intrinsic and Robust Nature of Van Hove Singularities in Twisted Bilayer Graphene by Scanning Tunneling Microscopy and Theoretical Analysis, Phys. Rev. Lett. **109**, 196802 (2012).

[40] M. Karalic, S. Mueller, C. Mittag, K. Pakrouski, Q. S. Wu, A. A. Soluyanov, M. Troyer, T. Tschirky, W. Wegscheider, K. Ensslin, and T. Ihn, Experimental signatures of the inverted phase in InAs/GaSb coupled quantum wells, Phys. Rev. B **94**, 241402(R) (2016).

[41] I. Knez, R. R. Du, and G. Sullivan, Finite conductivity in mesoscopic Hall bars of inverted InAs/GaSb quantum wells, Phys. Rev. B **81**, 201301(R) (2010).

[42] K. Suzuki, Y. Harada, K. Onomitsu, and K. Muraki, Edge channel transport in the InAs/GaSb topological insulating phase, Phys. Rev. B **87**, 235311 (2013).

[43] S. Mueller, A. N. Pal, M. Karalic, T. Tschirky, C. Charpentier, W. Wegscheider, K. Ensslin, and T. Ihn, Nonlocal transport via edge states in InAs/GaSb coupled quantum wells, Phys. Rev. B **92**, 081303(R) (2015).

[44] S. Mueller, C. Mittag, T. Tschirky, C. Charpentier, W. Wegscheider, K. Ensslin, and T. Ihn, Edge transport in InAs and InAs/GaSb quantum wells, Phys. Rev. B **96**, 075406 (2017).

[45] B.-M. Nguyen, A. A. Kiselev, R. Noah, W. Yi, F. Qu, A. J. Beukman, F. K. de Vries, J. van Veen, S. Nadj-Perge, L. P. Kouwenhoven, M. Kjaergaard, H. J. Suominen, F. Nichele, C. M. Marcus, M. J. Manfra, and M. Sokolich, Decoupling Edge versus Bulk Conductance in the Trivial Regime of an InAs/GaSb Double Quantum Well using Corbino Ring Geometry, Phys. Rev. Lett. **117**, 077701 (2016).

[46] V. Sazgari, G. Sullivan, and I. I. Kaya, Localization of trivial edge states in InAs/GaSb composite quantum wells, Phys. Rev. B **100**, 041404(R) (2019).

[47] E. M. Spanton, K. C. Nowack, L. Du, G. Sullivan, R.-R. Du, and K. A. Moler, Images of Edge Current in InAs/GaSb Quantum Wells, Phys. Rev. Lett. **113**, 026804 (2014).

[48] F. Nichele, H. J. Suominen, M. Kjaergaard, C. M. Marcus, E. Sajadi, J. A. Folk, F. Qu, A. J. A. Beukman, F. K. de Vries, J. van Veen, S. Nadj-Perge, L. P. Kouwenhoven, B.-M. Nguyen, A. A. Kiselev, W. Yi, M. Sokolich, M. J. Manfra, E. M. Spanton, and K. A. Moler, Edge transport in the trivial phase of InAs/GaSb, New J. Phys. **18**, 083005 (2016).

[49] S. Kaku, T. Ando, and J. Yoshino, Real space imaging of topological edge states in InAs/GaSb and InAs/$In_xGa_{1-x}Sb$ quantum wells, ACS Nano **13**, 12980 (2019).

[50] F. Qu, A. J. A. Beukman, S. Nadj-Perge, M. Wimmer, B.-M. Nguyen, W. Yi, J. Thorp, M. Sokolich, A. A. Kiselev, M. J. Manfra, C. M. Marcus, and L. P. Kouwenhoven, Electric and Magnetic Tuning Between the Trivial and Topological Phases in InAs/GaSb Double Quantum Wells, Phys. Rev. Lett. **115**, 036803 (2015).

[51] S. S. Krishtopenko and F. Teppe, Realistic picture of helical edge states in HgTe quantum wells, Phys. Rev. B **97**, 165408 (2018).

[52] F. Couëdo, H. Irie, K. Suzuki, K. Onomitsu, and K. Muraki, Single-edge transport in an InAs/GaSb quantum spin Hall insulator, Phys. Rev. B **94**, 035301 (2016).